

47 **Abstract**

48 The coplane analysis technique for mapping the three-dimensional wind field of
49 precipitating systems is applied to the NASA High Altitude Wind and Rain Airborne Profiler
50 (HIWRAP). HIWRAP is a dual-frequency Doppler radar system with two downward pointing
51 and conically scanning beams. The coplane technique interpolates radar measurements to a
52 natural coordinate frame, directly solves for two wind components, and integrates the mass
53 continuity equation to retrieve the unobserved third wind component. This technique is tested
54 using a model simulation of a hurricane and compared to a global optimization retrieval. The
55 coplane method produced lower errors for the cross-track and vertical wind components, while
56 the global optimization method produced lower errors for the along-track wind component.
57 Cross-track and vertical wind errors were dependent upon the accuracy of the estimated
58 boundary condition winds near the surface and at nadir, which were derived by making certain
59 assumptions about the vertical velocity field. The coplane technique was then applied
60 successfully to HIWRAP observations of Hurricane Ingrid (2013). Unlike the global
61 optimization method, the coplane analysis allows for a transparent connection between the radar
62 observations and specific analysis results. With this ability, small-scale features can be analyzed
63 more adequately and erroneous radar measurements can be identified more easily.

64

65

66

67

68

69

70 **1. Introduction**

71 The use of airborne Doppler radars has significantly advanced our understanding of
72 meteorological phenomena by providing wind structure information that details the dynamics of
73 an evolving system. Airborne platforms have been particularly important for observing
74 phenomena that occur in remote areas, such as tropical cyclones over the open ocean. Lhermitte
75 (1971) first discussed the idea of using airborne Doppler radars for obtaining three-dimensional
76 wind structures. A single Doppler radar beam measures the along-beam velocity component of
77 precipitation particles within that beam. In order to retrieve all three components of the wind
78 field, two (or more) Doppler radar beams must scan an area with a sufficient separation angle
79 between the beams (e.g. Armijo 1969; Klimowski and Marwitz 1992). Airborne radars must
80 therefore employ certain scanning techniques that provide multiple views of the wind from
81 sufficiently different angles in order to map the wind structure of the precipitation phenomena.

82 In one of the first airborne Doppler studies, Marks and Houze (1984) utilized a scanning
83 technique for successful mapping of the three-dimensional wind field. They used data collected
84 by the X-band Doppler radar on board the National Oceanic and Atmospheric Administration's
85 (NOAA) WP-3D (P3) aircraft. Located in the tail of the aircraft, the radar antenna pointed
86 orthogonally to the aircraft track and scanned circularly through all elevation angles around a
87 horizontal axis (for more on this radar, see Jorgensen 1984). Multiple viewing angles of the same
88 domain were obtained by flying the aircraft at different track angles. Another tail radar was later
89 installed on the second NOAA P3 aircraft allowing for simultaneous Doppler observations when
90 both aircraft were flown together (Gamache et al. 1995). Both tail radars soon implemented the
91 fore/aft scanning technique (FAST; Jorgensen and DuGranrut 1991), in which the antenna
92 alternately points $\sim 20^\circ$ to the fore and aft of the aircraft while circularly sweeping around a

93 horizontal axis. With this technique, multiple along-beam velocity measurements from the same
94 domain are obtained along a single flight track by the different fore and aft angles. The National
95 Center for Atmospheric Research (NCAR) Electra Doppler Radar (ELDORA) operates with the
96 same scanning geometry but utilizes two antennas that rotate at a faster rate, allowing for higher
97 resolution observations (Hildebrand et al. 1996).

98 Multiple techniques for retrieving the three-dimensional wind field have been developed
99 for the NOAA P3 tail radar and the ELDORA radar, which both scan around a horizontal axis.
100 The first method is a local solver that interpolates radial velocities from each viewing angle to a
101 Cartesian grid and solves for the corresponding velocities in the horizontal plane. These
102 horizontal velocities from different viewing angles are then used to calculate two orthogonal
103 horizontal wind components (e.g. Jorgensen et al. 1983; Marks and Houze 1984). The vertical
104 wind component is calculated by integrating the anelastic mass continuity equation using
105 appropriate boundary conditions. This technique is simple and computationally inexpensive, but
106 errors can accumulate in the wind component along the direction of integration (Gao et al. 1999).

107 The second method is a global optimization approach that minimizes a cost function
108 containing the differences between the radar-measured and retrieved velocity components. This
109 cost function also includes constraints such as the anelastic mass continuity equation and vertical
110 velocity boundary conditions (Gamache 1997; Bousquet and Chong 1998; Reasor et al. 2009).
111 With the avoidance of explicit integration, this variational technique reduces errors in the vertical
112 velocity for the aforementioned scanning geometry (Gao et al. 1999). Since all retrieval
113 strategies are limited by the geometry of the scanning technique, no individual retrieval method
114 is perfect; however, utilizing multiple methods adds to the reliability of scientific interpretations
115 of retrieved wind fields.

116 The High-Altitude Imaging Wind and Rain Airborne Profiler (HIWRAP), recently
117 developed at NASA Goddard Space Flight Center, is a Doppler radar system that employs a
118 different scanning strategy from the previously mentioned airborne Doppler radars (Li et al.
119 2014). It operates with two beams that point downward at fixed angles (30° and 40° away from
120 nadir) with each beam scanning conically around a vertical axis. HIWRAP flew for the first time
121 in 2010 on the NASA Global Hawk unmanned aircraft during the Genesis and Rapid
122 Intensification Processes (GRIP) field experiment (Braun et al. 2013).

123 Recent studies have begun exploring how established retrieval methods can be applied to
124 the scanning geometry of HIWRAP. Tian et al. (2015) applied the Velocity Azimuth Display
125 (VAD) technique (Lhermitte and Atlas 1961; Browning and Wexler 1968) to HIWRAP data to
126 obtain the mean vertical profile of the horizontal wind along the flight track. Under the
127 assumptions that the wind field is linear and the vertical velocity is constant across the scan
128 circle, this method fits the measured radial winds at each altitude to a sinusoidal curve as a
129 function of azimuth. Guimond et al. (2014) implemented the global optimization technique to
130 obtain the three-dimensional wind field in the HIWRAP scanning domain. The cost function for
131 this variational scheme included a modified weighting parameter that was better suited for the
132 different scanning geometry.

133 In this paper, we extend the application of established retrieval techniques to the
134 HIWRAP geometry by focusing on a simple interpolation and integration approach. The vertical
135 integration scheme used for the P3 tail radars cannot be applied in the HIWRAP case since the
136 scanning geometry does not align sufficiently with the horizontal wind in order to avoid large
137 projection errors introduced by the vertical wind. A better alternative is the coplane method
138 described by Armijo (1969) and Miller and Strauch (1974). The coplane method uses a

139 cylindrical coordinate system in which two components of the wind are readily derived from the
140 observations. The third wind component is completely unobserved by the radar and must be
141 retrieved by explicitly integrating the mass continuity equation with specified boundary
142 conditions. As a local solver, the solution of the coplane method at a certain gridpoint has a
143 transparent relationship to the local radar observations, whereas in a global solver, observations
144 across the radar domain have an impact on the solution at an individual grid point. Without such
145 interference, possible errors in the radar measurements or retrieved winds are more easily
146 identifiable and traceable. With a natural coordinate system, the coplane method is particularly
147 useful for understanding the advantages and disadvantages of the HIWRAP scanning technique.
148 This understanding is necessary for interpreting any Doppler analysis method used on the
149 HIWRAP radar geometry. In this study, we apply the coplane technique to simulated radar data
150 and actual radar data to demonstrate its effectiveness. We also compare this technique to the
151 global optimization solutions and investigate their differences.

152 Sections 2-3 describe the coplane method and its application to the HIWRAP geometry
153 and observations. Section 4 examines the boundary conditions necessary for the coplane method.
154 Section 5 analyzes the coplane retrieval of simulated radar data and Section 6 analyzes the
155 coplane retrieval of real HIWRAP data. Finally, Section 7 presents the conclusions of this study.

156

157 **2. Coplane method and HIWRAP geometry**

158 *a. Description of HIWRAP*

159 HIWRAP is a dual-beam, dual-frequency (Ka and Ku band) radar system designed to fly
160 on the high-altitude NASA Global Hawk unmanned aircraft system. Rather than scanning around
161 a horizontal axis like the tail radars on the P3 aircraft, the antenna beams of HIWRAP point

162 downward and scan around a vertical axis to obtain multiple angled looks of the tropospheric
163 winds. Figure 1 illustrates this scanning geometry. The two beams point at nominal tilt angles (τ)
164 of 30° and 40° away from nadir, while the antenna rotates at a typical rate of 100° per second,
165 such that one complete revolution takes about 3.5 s. The radar beams, each with a range
166 resolution of 150 m, sweep out spiral paths on the ground as the aircraft flies with an ideal level
167 position along a straight flight track. For a typical aircraft speed of 160 m s^{-1} and altitude of 18.5
168 km, the along-track sampling and swath width are 560 m and ~ 30 km respectively. The outer
169 beam operates simultaneously at 13.5 and 33.7 GHz and the inner beam operates simultaneously
170 at 13.9 and 35.6 GHz. HIWRAP employs dual pulse repetition frequency sampling that can yield
171 an extended unambiguous velocity of $\sim 110 \text{ m s}^{-1}$. A more detailed description of HIWRAP can
172 be found in Li et al. (2014).

173

174 *b. Description of coplane method*

175 The coplane dual-Doppler technique was developed to retrieve the three-dimensional
176 winds with two or more ground radars (Armijo 1969; Miller and Strauch 1974) and later applied
177 to airborne tail radars employing the FAST scanning technique (Chong and Testud 1996). This
178 technique is implemented in a cylindrical coordinate system whose central axis is the line
179 between the location points where the radar (or radars) provides two different looks of a single
180 point in the domain. For aircraft observations, the ideal situation for the coplane method would
181 have a straight flight track and constant flight altitude across the analysis domain. The two looks
182 of the wind field, obtained with fore and aft pointing beams, are considered independent and, for
183 the purpose of this study, instantaneous. For the typical Global Hawk speed and altitude, the
184 largest time gap between the observations is 200 s. These two measurements can then be readily

185 converted into two orthogonal wind components. Recovery of the third wind component at every
 186 point in the domain requires well-posed data (i.e., data exists at every point). To describe the
 187 application of the coplane method to the downward pointing conically scanning HIWRAP
 188 geometry, we follow the discussions from Tian et al. (2015) and Guimond et al. (2014).

189 Figure 2 illustrates the cylindrical coordinate system defined by ρ , α , and Y . The flight
 190 track serves as the main axis Y where the origin is some arbitrary point along Y . The variable ρ is
 191 the radial distance from the central axis, and α is the coplane angle beginning at 0° for the nadir
 192 plane and increasing to the right of the flight track. For every rotation angle θ (0° points in $+Y$
 193 direction), range r , and current track position Y_1 , observations are first mapped onto a track-
 194 following Cartesian grid by

$$\begin{pmatrix} X_t \\ Y_t \\ Z_t \end{pmatrix} = r \begin{pmatrix} \cos D(a) - \sin D \sin \tau(b) - \sin D(c) \\ Y_1/r + \sin D(a) + \cos D \sin \tau(b) + \cos D(c) \\ \sin \tau (\sin P \cos \theta - \cos P \sin R \sin \theta) - \cos P \cos R \cos \tau \end{pmatrix} \quad (1)$$

195 where

$$\begin{pmatrix} a \\ b \\ c \end{pmatrix} = \begin{pmatrix} \cos R \sin \theta \sin \tau - \sin R \cos \tau \\ \cos P \cos \theta + \sin P \sin R \sin \theta \\ \sin P \cos R \cos \tau \end{pmatrix} \quad (2)$$

196 and D , P , R and τ are the drift, pitch, roll and tilt angles, respectively. Equations (1) and (2) are
 197 similar to Guimond et al. (2014) and are derived for the current scanning geometry following
 198 Lee et al. (1994). The cylindrical coordinates of the observations are then calculated by

$$\begin{pmatrix} \rho \\ \alpha \\ Y \end{pmatrix} = \begin{pmatrix} \sqrt{X_t^2 + Z_t^2} \\ \tan^{-1} \left(\frac{X_t}{Z_t} \right) \\ Y_t \end{pmatrix}. \quad (3)$$

199 As the plane flies along the track, a single beam at a given tilt angle τ obtains Doppler
 200 velocities in an α plane when it is located at Y_1 (fore) and Y_2 (aft). These velocities are

201 interpolated to the cylindrical coordinate grid so that each grid point P contains consolidated fore
 202 and aft radial velocities (V_{r1} , V_{r2} respectively) as seen in Fig. 2. Orthogonal velocities in the α
 203 plane are then calculated by

$$U_\rho = \frac{-r_1(Y - Y_2)V_{r1} + r_2(Y - Y_1)V_{r2}}{\rho(Y_2 - Y_1)} \quad (4)$$

$$U_Y = \frac{r_1V_{r1} - r_2V_{r2}}{Y_2 - Y_1}$$

204 where $r_1 = \sqrt{\rho^2 + (Y - Y_1)^2}$ and $r_2 = \sqrt{\rho^2 + (Y - Y_2)^2}$. From these standard dual-Doppler
 205 calculations, we obtain two velocity components (U_ρ , U_Y) in each α plane of the cylindrical grid.

206 The separation angle β , defined as $\beta = \beta_1 + \beta_2$ as seen in Fig. 2, is the angle between the
 207 fore and the aft beams. The angles β_1 and β_2 are calculated by

$$\beta_n = \sin^{-1}(|Y - Y_n|/r_n) \quad (5)$$

208 where β_n represents either β_1 or β_2 . Combining Eqs. (1)-(3) and assuming all attitude angles are
 209 equal to 0, Eq. (5) can be rewritten as

$$\beta_n = \sin^{-1}(\cos \tau_e \cos(\sin^{-1}(\tan \tau_e \tan \alpha))) \quad (6)$$

210 where β_n is now a function of the coplane angle α . Eq. (6) uses the elevation angle τ_e which is
 211 defined as $\tau_e = \tau - 90^\circ$. The separation angle directly corresponds to the accuracies of the two
 212 retrieved wind components, U_ρ and U_Y . In applying the error estimates of Doviak et al. (1976)
 213 and trigonometric substitutions to Eq. (4), the variances of the two wind components are
 214 specified by

$$\sigma_\rho^2 = \frac{\sigma_{r1}^2 + \sigma_{r2}^2}{4 \cos^2 \beta_1} \sigma_Y^2 = \frac{\sigma_{r1}^2 + \sigma_{r2}^2}{4 \sin^2 \beta_1} \quad (7)$$

215 where σ_{r1} and σ_{r2} are the errors of V_{r1} and V_{r2} . The errors σ_{r1} and σ_{r2} are equal to each other
 216 given that V_{r1} and V_{r2} are independent measurements. Tian et al. (2015) determined that the

217 standard error of HIWRAP Doppler estimates for the Ka band is $\sigma_r = 0.46 \text{ m s}^{-1}$. Eq. (7) assumes
218 that all errors are Gaussian distributed. Other sources of error can contribute to σ_r such as
219 velocity unfolding error and error due to aircraft motion. For the analysis in Section 6, we
220 verified that the Doppler velocities were unfolded properly. The Doppler velocities were also
221 corrected for aircraft motion using attitude information (i.e. roll, drift, and pitch).

222 Figure 3 shows the separation angle and the corresponding wind variances as a function
223 of the coplane angle for the two tilt angles of the HIWRAP geometry. It is shown that β reaches
224 its peak at nadir and then decreases as α increases in magnitude. σ_Y^2 is lowest at nadir and
225 remains below $0.6 \text{ m}^2 \text{ s}^{-2}$ throughout most of the domain. Towards the domain edges, the fore and
226 aft beams become closely parallel (i.e. β approaches 0°) and point less in the along-track
227 direction. Consequently, the accuracy of the retrieved U_Y quickly degrades at large α magnitudes.
228 On the other hand, the U_ρ component is accurately estimated ($\sigma_\rho^2 < 0.2 \text{ m}^2 \text{ s}^{-2}$). It is most
229 accurate near the domain edges and least accurate at nadir. Still, the magnitudes of σ_ρ^2 and its
230 corresponding changes with α are lower than that of σ_Y^2 . Studies have shown that the two in-
231 plane wind components can both be retrieved with reasonable accuracy when the separation
232 angle is at least 30° (e.g. Klimowski and Marwitz 1992). In this scanning geometry, the outer
233 beam retrieves the wind components with reasonable accuracy when $|\alpha| < 37.5^\circ$ where
234 $\sigma^2 < 1.56 \text{ m}^2 \text{ s}^{-2}$ for both components.

235 Figure 3 also shows that the outer beam retrieves U_Y more accurately while the inner
236 beam retrieves U_ρ more accurately within its smaller domain. We incorporate observations from
237 both beams by weighting these relative retrieval accuracies. For each gridpoint within the
238 domain of the inner beam, the composite wind components are

$$U_\rho = \frac{\sigma_{\rho i}^2 U_{\rho o} + \sigma_{\rho o}^2 U_{\rho i}}{\sigma_{\rho i}^2 + \sigma_{\rho o}^2} \quad (8)$$

$$U_Y = \frac{\sigma_{Y i}^2 U_{Y o} + \sigma_{Y o}^2 U_{Y i}}{\sigma_{Y i}^2 + \sigma_{Y o}^2}$$

239 where the i and o subscripts denote observations from the inner and outer beams.

240 The third component of the wind, U_α , is retrieved by integrating the anelastic mass
 241 continuity equation along the α -axis away from the nadir plane. Figure 4 illustrates the two
 242 integration directions that span the radar domain. The anelastic mass continuity equation is given
 243 by

$$\frac{\partial(\rho\eta U_r)}{\partial\rho} + \frac{\partial(\eta U_\alpha)}{\partial\alpha} + r \frac{\partial(\eta U_Y)}{\partial Y} = 0 \quad (9)$$

244 where η is the air density. The current calculations use the Jordan (1958) standard Tropical
 245 Atlantic air density profile. Using the square rule for integration on Eq. (9), U_α is obtained by

$$\eta U_\alpha \Big|_{\alpha_1} = \eta U_\alpha \Big|_{\alpha_0} - \frac{1}{2}(\alpha_1 - \alpha_0)(f(\alpha_1) + f(\alpha_0)) \quad (10)$$

$$f(\alpha) = \frac{\partial(\rho\eta U_r)}{\partial\rho} + r \frac{\partial(\eta U_Y)}{\partial Y}$$

246 where the subscripts 0 and 1 denote the previous and current integration locations. As depicted in
 247 Fig. 4, U_α must be initialized with boundary conditions at the nadir plane and at the surface. In
 248 order to retrieve U_α at all points, the data must exist at all points in the domain. If radial
 249 velocities are missing at any point, U_α cannot be calculated at points along the integration path
 250 beyond the missing point. Data may continue beyond the missing point allowing for calculation
 251 of U_Y and U_ρ .

252 The nadir boundary condition is obtained by taking observations at small angles away
 253 from nadir on either side. In the track-following Cartesian grid, the Cartesian coordinate cross-

254 track (u), along-track (v), and vertical (w) velocities are related to the cylindrical coordinate
 255 velocities by

$$U_\rho = u \sin \alpha - w \cos \alpha \quad (11)$$

$$U_Y = v \quad (12)$$

$$U_\alpha = u \cos \alpha + w \sin \alpha \quad (13)$$

256 Suppose that U_ρ components ($U_{\rho 1}, U_{\rho 2}$) are calculated at a small angle α on either side of nadir
 257 ($\alpha_1 = +\alpha; \alpha_2 = -\alpha$) at a constant radius. For the two U_ρ components, we make the assumption
 258 that w is constant and u is linear across the span of the U_ρ locations. It follows from Eq. (11) that
 259 u at nadir (u_0) is expressed by

$$u_0 = \frac{U_{\rho 1} - U_{\rho 2}}{2 \sin \alpha} \quad (14)$$

260 for each altitude corresponding to the radius of the U_ρ observations. Since $U_\alpha = u_0$ at nadir, Eq.
 261 (14) gives the boundary condition for initializing U_α along the nadir plane. To calculate the nadir
 262 boundary condition, we chose a value of $\alpha = 3.35^\circ$ for the outer beam and $\alpha = 2.31^\circ$ for the
 263 inner beam. The two u_0 values from each beam at each point are combined according to the U_ρ
 264 calculation and error estimates from Eq. (8). This weighting was selected since the final values
 265 rely on U_ρ calculations.

266 At the surface, the impermeability condition ($w = 0$) is applied as a boundary condition.
 267 By setting w equal to 0, Eqs. (11) and (13) lead to

$$U_\alpha \Big|_{z=0} = U_\rho / \tan \alpha \quad (15)$$

268 With this relationship, U_ρ can be used to initialize U_α at the surface. The surface boundary
 269 condition works well in an idealized setting where accurate observations are available near the
 270 surface and the surface is flat. However, in actual aircraft observations over water, sea spray can

271 contaminate the Doppler measurements and the surface is not flat. We address these surface
272 issues and assess the nadir boundary condition in Section 4.

273

274 **3. Data and methods**

275 *a. Radar simulator*

276 In order to assess the validity of the coplane analysis, we use model output and a radar
277 simulator designed after Guimond et al. (2014) with no added noise or aircraft attitude. The radar
278 simulator mimics the scanning technique of the HIWRAP radar and obtains radial velocities V_r
279 from the modeled velocity fields as the radar moves along a straight level track. The model used
280 is the nonhydrostatic fifth-generation Penn State University– National Center for Atmospheric
281 Research Mesoscale Model (MM5). We take an MM5 simulation of Hurricane Rita (2005) at a
282 single time frame near its peak intensity (maximum wind speed of 75 m s^{-1}). The model output
283 has a horizontal resolution of 1.67 km and 28 sigma levels in the vertical. Two simulated radar
284 beams are positioned at 30° and 40° tilt angles, and rotate at a period of 3.5 seconds per
285 revolution with an azimuthal resolution of 2° and a range resolution of 150 m. The radar has a
286 nominal altitude of 18.5 km and the simulated aircraft has a ground speed of 160 m s^{-1} . Shown in
287 Fig. 5, the track has a length of 200 km and passes through the center of the storm.

288

289 *b. Real data*

290 On 16 September 2013, the NASA Global Hawk AV-1 flew over Hurricane Ingrid as part of
291 the NASA Hurricane and Severe Storm Sentinel (HS3) field campaign. The HIWRAP radar
292 on board the Global Hawk observed the northern edge of Ingrid as the storm tracked west
293 across the Gulf of Mexico. The data used in this study were taken from 1836-1900Z. Figure 6

294 shows the HIWRAP observed reflectivity (plan view and at nadir) along with the
 295 corresponding infrared satellite image. In Section 6, we apply the coplane analysis to the Ka-
 296 band outer beam observations. To remove noise, pixels with reflectivity less than 0 dBZ were
 297 not used in the analysis. The Doppler velocities were unfolded according to Dazhang et al.
 298 (1984). We applied corrections for beam pointing errors by aligning the expected range of
 299 the ocean surface with the range of the observed surface return. Fall speed corrections from
 300 Heymsfield et al. (2010) were also applied to the velocity data. In this correction algorithm,
 301 fall speeds were calculated as a function of the Ka band reflectivity and altitude.

302 *c. Grid and interpolation specifications*

303 The coplane method requires an initial interpolation of radial velocity data to a
 304 cylindrical grid. The cylindrical grid used in this study has a radial resolution of 0.5 km, along-
 305 track resolution of 2 km, and azimuthal resolution of 2.5°. The observations (both simulated and
 306 real) are interpolated to this grid using a Barnes weighting scheme (Barnes 1973; Koch et al.
 307 1983) given by

$$w_m = \exp\left(-\left[\frac{r_m}{\gamma\delta}\right]^2\right) \quad (16)$$

308 where r_m is the distance of the m^{th} observation from the analysis grid point, γ is a chosen shape
 309 parameter, and δ is the influence radii expressed by

$$\delta = \sqrt{r_\rho^2 + r_Y^2 + r_\alpha^2} \quad (17)$$

310 where r_ρ , r_Y , and r_α are the radii of influence in the three coordinate directions. For this
 311 interpolation, the radial, horizontal, and azimuthal radii of influence are 0.5 km, 2 km, and 1.25°
 312 respectively. The 1.25° azimuthal radius of influence has an equivalent distance of 2 km and the
 313 shape parameter γ , which determines the width of the weighting function, is chosen as 0.75.

314 Following the coplane calculations, the data are converted into Cartesian coordinate velocities
315 via Eqs. (11)-(13) and are finally interpolated to Cartesian coordinates. The Cartesian grid has a
316 horizontal resolution of 2 km and a vertical resolution of 1 km. An additional level is added at
317 0.5 km altitude for better resolving of the low-level winds. This interpolation uses the same
318 Barnes filter but with a radius of influence of 2 km in the horizontal dimensions and 0.25 km in
319 the vertical in the vertical dimension. By determining the response function of the Barnes filter
320 (Koch et al. 1983), the minimum resolvable horizontal wavelength is calculated to be 4 km,
321 which is also twice the horizontal grid spacing.

322

323 **4. Boundary conditions analysis**

324 *a. Nadir boundary condition analysis*

325 At nadir, the cross-track wind component is unobserved by the HIWRAP radar and must
326 be estimated by utilizing other available measurements. It is important to obtain a good estimate
327 of the cross-track wind at nadir as this will serve as the boundary condition that initializes the U_α
328 wind component for integration throughout most of the domain. As shown in Eq. (14), we
329 estimate the cross-track wind by using wind measurements taken at a small angle α away from
330 nadir. Choosing a value for α requires a balance of certain trade-offs. For smaller α values, the
331 distance between observations is smaller and thus the assumptions of constant vertical velocity
332 and linear cross-track velocity are well suited. However, at angles that are closer to zero, the
333 wind measurements are more susceptible to errors in the cross-track velocity. For larger α
334 values, the cross-track wind is better sampled and this reduces the susceptibility to measurement
335 errors; however, the distance between observations is greater making the necessary assumptions
336 less suitable.

337 We use the simulated radar data to choose a value for α . Boundary condition estimates
338 are calculated with varying α values, which are then compared to the model “truth” cross-track
339 velocities. This calculation requires interpolation of radial velocities to the different α planes. A
340 Barnes filter is used for the interpolation with the influence radii specified in Section 3c.
341 Assuming all attitude angles are equal to zero, Eqs. (1)-(3) yield α as a function of the rotation
342 angle θ and the elevation angle τ_e :

$$\alpha = \tan^{-1} \left(\frac{\sin \theta \cos \tau_e}{\sin \tau_e} \right) \quad (18)$$

343 The α values are tested by varying the deviation of θ from the nadir plane. For example, the
344 rotation angles 2° and 178° lie in the plane $\alpha = 1.677^\circ$ for the outer beam. Correspondingly, the
345 rotation angles 358° and 182° lie in the plane $\alpha = -1.677^\circ$. Figure 7a shows the coplane angles
346 for the varying rotation angle, while Figure 7b presents the root-mean-square (RMS) errors for
347 the different estimates. The errors are all relatively small compared to the wind speeds of the
348 simulated hurricane. For a wind speed of 30 m s^{-1} , the largest error in Fig. 7b constitutes 5% of
349 this wind speed. The α values corresponding to $\theta = 4^\circ$ produced the smallest error, so we
350 chose these values for the boundary condition retrieval. As seen in Fig. 7b, the angle $\theta = 4^\circ$
351 corresponds to a cross-track distance between observations of 2.2 km at the surface.

352 Figure 8 displays the estimated U_α at nadir along with the errors relative to the model
353 truth. The retrieved wind field captures the overall structure of the hurricane. Errors larger than 2
354 m s^{-1} occur near the eyewall region ($Y = 85$ and 115 km), the surface, and the domain edge at $Y =$
355 18 km . These positive errors at the domain edge reach 8 m s^{-1} . The largest negative errors occur
356 in the midlevels near $Y = 155 \text{ km}$ reaching values of -9 m s^{-1} . These errors stem from local
357 violations of the assumptions made in the calculation of Eq. (14). Specifically, violations of the

358 constant vertical velocity assumption are the primary source of error in Fig. 8, where vertical
359 velocity deviations of 0.5 m s^{-1} produced U_α errors of $\sim 3 \text{ m s}^{-1}$.

360

361 *b. Surface boundary condition analysis*

362 The values of U_α must be initialized at the lower boundary of the analysis domain. Given
363 the curved paths of integration, this initialization affects the lower portion of the domain that
364 increases in depth away from nadir (as indicated in Fig. 4). As described in Section 2, the lower
365 boundary initialization can be done most simply by invoking the impermeability condition and
366 setting $w = 0$ at the surface (Eq. 15). This condition requires reliable observations near a flat
367 surface, which is an ideal situation that models provide. The initialization locations on the
368 surface are not necessarily points on the cylindrical grid, but U_α can still be effectively initialized
369 for every integration path that intersects the surface.

370 With actual observations, setting the surface boundary condition cannot be done so
371 simply, particularly over the ocean surface as in the case of tropical cyclone research. The ocean
372 surface may not be flat and sea spray can contaminate echoes near the surface. Previous dual-
373 Doppler methods approach the surface initialization of the integrated wind component (usually
374 w) differently. In the Cartesian Editing and Display of Radar Data under Interactive Control
375 software (CEDRIC; Mohr et al. 1986), the vertical velocity can be initialized at the lowest level
376 of usable data by setting w equal to a specified multiple of the locally measured horizontal
377 divergence. Chong and Testud (1996) use a variational method in which w at all surface
378 locations vary near $w = 0$ such that the resulting U_α field contains a minimum amount of
379 continuity irregularities.

380 For this study, we use a simple approach that initializes U_α at the lowest cylindrical grid
 381 points closest to a selected low-level altitude. In the simulated data, we choose 0.5 km as the
 382 lowest level of available data, which is approximately the lowest level of usable data from the
 383 HIWRAP observations. For this cylindrical coordinate system, the lower boundary grid points
 384 are not all at the same altitude. By combining Eqs. (11) and (13), U_α at each lower boundary
 385 point is given by

$$U_\alpha = \frac{U_\rho}{\tan \alpha} + w \left(\frac{\cos^2 \alpha}{\sin \alpha} + \sin \alpha \right) \quad (19)$$

386 Using this equation, U_α is initialized with the local U_ρ . Additionally, we estimate w from the
 387 vertical velocity calculated at nadir (where $w = -U_\rho$) for that corresponding altitude and Y
 388 location.

389 The calculated lower bound U_α values were compared to the model truth and resulted in
 390 an RMS error of 2.05 m s^{-1} . Moreover, the lower bound U_α values stemming from the original
 391 impermeability condition resulted in an RMS error of 1.69 m s^{-1} . As expected, the accuracy of
 392 the nadir- w approach is slightly lower than that of the impermeability approach; however, the
 393 difference in the errors (0.36 m s^{-1}) is small relative to the near-surface hurricane wind speeds
 394 (which have magnitudes greater than 30 m s^{-1} outside the eye. From this analysis, the nadir- w
 395 approach represented by Eq. (19) is deemed suitable for U_α initialization for near-surface grid
 396 points.

397

398 **5. Retrieval error analysis**

399 In this section, we use the simulated radar data to examine the wind field retrieved from
 400 the coplane analysis. As described in the previous section, we do not use radar radial velocities
 401 below 0.5 km altitude in this retrieval. Figures 9a-c present the RMS errors calculated along the

402 flight track for the retrieved cross-track (u), along-track (v), and vertical velocity (w)
403 components. These figures show the total errors and the error patterns of each wind component
404 for the HIWRAP scanning geometry. The total relative-RMS (RRMS) error in each figure is a
405 normalization of the errors relative to the velocity magnitudes.

406 The cross-track component (u) contains an average error of 1.9 m s^{-1} which, as indicated
407 by the relative-RMS value of 4.4%, is a low error compared to the u magnitudes. Calculation of
408 u depends on both the U_α and U_ρ components, but the u errors largely stem from errors in U_α as
409 this component is larger and more aligned with u throughout the domain. The u errors form a
410 curved pattern as they follow the integration path upon which U_α was calculated. The largest
411 errors occur near the surface and in a midlevel belt positioned between 4-6 km altitude at nadir.
412 The vertical velocity (w) contains an average error of 0.9 m s^{-1} which is significant relative to the
413 vertical velocity magnitudes (RRMS = 60.4%). Despite this significant average error, the error
414 distribution in Fig. 9c shows that the vertical velocities near nadir have the smallest errors and
415 therefore are the most useful. The errors increase as the α angle magnitude increases toward the
416 edges of the domain, with particularly large magnitudes at locations that coincide with the u error
417 belt in Fig. 9a. At these larger α angles, U_α makes an increasing contribution to determining w .
418 As a result, U_α errors that are small relative to the horizontal winds can lead to significant w
419 errors near the domain edges.

420 We have explained that errors in the u and w fields are mostly due to U_α errors. These
421 errors in the U_α component accumulate during the integration of the wind field for two reasons.
422 First, the divergence of the wind field in the α planes is not well sampled, particularly near the
423 domain edges where U_Y calculations become less accurate (Fig 3b). Second, U_α is incorrectly
424 initialized for the two boundary conditions. We briefly test which reason is most responsible for

425 the U_α errors by substituting the lower bound and nadir U_α estimates with the model truth.
426 Figure 10 shows the RMS error patterns. Having the best initialization possible, the wind field
427 errors are significantly reduced to 1.1 m s^{-1} for u and 0.5 m s^{-1} for w . The u error no longer
428 contains the belted pattern and the corresponding w errors along the domain edges are removed.
429 This analysis suggests that the errors in the u and w wind fields are mostly a result of errors in
430 the boundary conditions. The remaining errors are less pronounced in Fig. 10 and can be
431 attributed to divergence sampling and interpolation error.

432 The along-track component (v) is the only Cartesian coordinate component that is not
433 calculated with the U_α component. The v errors are very small throughout most of the domain.
434 The largest errors, reaching up to 5 m s^{-1} , occur at 0.5 km altitude. These errors at the lowest
435 level are largely a result of the interpolation from cylindrical to Cartesian coordinates. The lower
436 bound points on the cylindrical grid are at different altitudes and are all higher than the 0.5 km
437 level. Since the data below 0.5 km were not used, these lower bound points are the only source
438 of information for interpolation onto the 0.5 km level, which contributes to errors found at this
439 lowest level for all Cartesian wind components. In this particular dataset, the v component
440 (which is largely the radial wind of the hurricane) changes very rapidly at these boundary layer
441 altitudes, resulting in the significant errors found in the lowest levels. When the 0.5-km-level
442 data are excluded from the error analysis, the RMS error drops from 1.7 m s^{-1} to 1.0 m s^{-1} .

443 The coplane analysis is now compared to the global optimization analysis described by
444 Guimond et al. (2014). In their variational method, radar velocities are first interpolated to a
445 Cartesian grid, and then a modeled wind field is retrieved using the radar velocities, mass
446 continuity, and boundary conditions as constraints. We applied the variational method to the

447 current simulated data using analysis parameters that produced the smallest errors. Specific
448 parameters that were chosen are listed in Table 1.

449 Figures 9d-f show the RMS errors for the three wind components. The u and w
450 components both have larger overall errors than the coplane analysis. These components, which
451 again are connected to each other through the unobserved wind component U_α , have error
452 patterns that are slightly different from the coplane analysis errors. The best retrievals occur at
453 nadir, and errors increase at all altitudes when approaching the domain edges. These error
454 patterns are consistent with those from Guimond et al. (2014). There is no belt of errors as in Fig.
455 9a, but increased errors do exist at nadir at the same altitude range of 4-6 km.

456 Meanwhile, the v field has a smaller overall error than the coplane analysis. The largest
457 difference in the v error pattern is in the lowest levels. The variational method operates fully in a
458 Cartesian coordinate system, which means that the lowest level of available data coincides with
459 the lowest level of grid points at 0.5 km altitude. As a result, the rapid vertical changes in v are
460 well captured at these levels and there is no interpolation error from changing coordinate
461 systems.

462

463 **6. Coplane retrieval with real radar data**

464 In the previous section, the coplane retrieval method was successfully applied to
465 simulated radar data. We now apply the coplane method to real HIWRAP data shown in Fig. 6
466 and we compare the retrieved wind field to a solution from the variational method (Guimond et
467 al. 2014).

468 Figures 11a-c presents the coplane analysis cross-track (u), along-track (v), and vertical
469 (w) components of the wind field along nadir of the observation domain. The u field contains

470 mostly positive velocities with values $> 10 \text{ m s}^{-1}$ in the layer below 3 km and the layer above 6
471 km. In between these layers a midlevel minimum of u occurs. The v field also contains mostly
472 positive velocities that decrease towards the upper levels of the domain (>7 km altitude). When
473 considering the domain location (Fig. 6a), the u and v fields show consistency with the counter-
474 clockwise cyclonic circulation of the storm. The cross-track component (Fig. 11a) largely
475 switches from positive to negative values at around $Y_t=230$ km which corresponds to the point
476 along the track that is closest to the storm center. Concurrently, the along-track component (Fig.
477 11b) increases as the track approaches the same closest point.

478 The reflectivity field shown in Fig. 6c contains a clear bright band signature (at ~ 4.5 km
479 altitude) and fall streaks, which indicate that the dominant precipitation regime for these
480 observations is stratiform (Houze 1997). In stratiform precipitation, falling ice crystals melt in a
481 layer beneath the 0° isotherm and form a broad region of light to moderate precipitation. The w
482 field (Fig 11c) shows consistent features with stratiform precipitation, including small
483 magnitudes ($< 2 \text{ m s}^{-1}$) throughout most of the domain. Updrafts are dominant above the bright
484 band. Below this level, downdrafts are prominent, but a clear exception of positive w values
485 occurs toward the beginning of the domain and at 4 km altitude. These exceptions, which are
486 inconsistent with typical stratiform kinematics, are likely a result of errors in the fall speed
487 correction and/or attenuation of the Ka beam. If these errors were consistent across the radial
488 velocities used in Eqs. (4) and (14) to calculate U_Y and u_0 , then the errors would not have an
489 impact on the fields in Figs. 11a and 11b.

490 Figures 12a-c present the wind components along a cross section at $Y_t=160$ km. These
491 cross sections show that the overall patterns seen at nadir extend to the edges of the domain. The
492 midlevel minimum of u grows larger to the right of the flight track (Fig. 12a). Additionally, the

493 downdraft layer (Fig. 12c) also increases in depth to the right of the flight track. The slanted
494 stretches of downdrafts $< -3 \text{ m s}^{-1}$ near the domain edges do not appear consistent with expected
495 vertical velocity patterns of stratiform precipitation. Rather, these patterns are reminiscent of the
496 curved error patterns in Figs. 9a and 9c. Given this resemblance, we infer that these w swaths
497 (and their corresponding u values) contain errors for the same reasons as in the radar simulator
498 analysis – that is, incorrect initializations of U_α at the boundary condition. By following the
499 curved α paths from these features towards the domain center, one finds that the boundary
500 condition errors occur at nadir between 1-2.5 km altitude in this cross section.

501 The variational method retrieved a qualitatively similar wind solution as that of the
502 coplane method. Figures 11d-f show that the u and v fields in the nadir plane have the same
503 overall structures as in Fig. 11a-c. Figure 11f mostly has the vertical velocities expected of
504 stratiform precipitation, but this solution takes the same fall speed corrections as in the coplane
505 method and produces noticeably different vertical velocities at the bright band altitude (~ 4.5
506 km). The variational u field (Fig. 11d) has noticeably smoother contour patterns than the coplane
507 u field (Fig. 11a), which suggests that the variational method may be filtering out some small-
508 scale features in the data. The v and w fields from both methods do not have a noticeable
509 discrepancy in their contour smoothness. Upon closer inspection, the u field at nadir is impacted
510 most by the smoothing parameter in the variational retrieval. When this smoothing parameter is
511 turned off, the resulting u field appears very similar to the coplane u field.

512 One advantage of the coplane method is that the minimum resolvable wavelength of the
513 data field is readily determined by calculating the response function of the Barnes filter. On the
514 other hand, determining the minimum resolvable wavelength of the variational method solution
515 is not as straight forward. While a Barnes filter is also used, the weighting parameter is a

516 *constraint* on the optimization and not a direct *calculation*. Thus the Barnes filter response
517 function cannot exactly determine the minimum resolvable wavelength. In addition, the
518 smoothing parameter certainly increases the minimum resolvable wavelength, but again, this
519 smoothing is a constraint and not a direct calculation. For both the Barnes filter and the
520 Laplacian smoother, the minimum resolvable wavelength must be determined empirically.

521 Figures 12d-f display the same cross section as in Figs. 12a-c but for the variational
522 solution. As in the coplane analysis, the midlevel u minimum and downdraft layer increase in
523 depth to the right of the flight track. The w field in Fig. 12f does not contain the unrealistic
524 downdraft patterns seen in Fig. 12c as there is no explicit integration along a curved path.
525 However, the w field does contain downdrafts $< -3 \text{ m s}^{-1}$ near the domain edges that appear
526 unrealistic. Along the left domain edge, these increased downdrafts occur in the same location as
527 in the coplane analysis (Fig. 12c). Along the right domain edge, these increased downdrafts are
528 prominent in the lower altitudes and appear to trail off into the higher altitudes. This pattern of
529 vertically oriented anomalies along the domain edge is reminiscent of the error pattern in Fig. 9f,
530 which suggest that these features contain likely errors. The source of these errors cannot be
531 traced to specific observations, but rather, the errors must be attributed to the general decreased
532 accuracy of the global solver along the domain edges.

533 Both the coplane and variational methods produced adequate wind fields that generally
534 agreed well with each other. Both fields also contained inevitable localized errors. With *a priori*
535 knowledge of the error patterns expected from each method, the questionable features that appear
536 in the solutions can be easily identified as retrieval errors. Identifying and understanding these
537 errors is essential for reliable scientific interpretations of solutions from either analysis method.

538 We make a final comparison of retrieval techniques to the VAD technique from Lin et al.
539 (2014). The VAD technique obtains the mean horizontal wind within the nadir plane by fitting
540 the measured radial winds in a scan circle to a sinusoidal curve. Figure 13 shows the retrieved u
541 and v components of the wind for the same leg of data from Hurricane Ingrid. The VAD
542 technique captures the same overall wind pattern that was retrieved by the other retrieval
543 techniques (Fig. 11). The most noticeable difference in Fig. 13 is the increased vertical
544 resolution. Since the VAD technique does not retrieve the full three-dimensional wind field, it is
545 computationally less expensive than both the coplane and variational methods; moreover, this
546 allows the VAD technique to preserve the high vertical resolution of the HIWRAP beam.
547 In calculating the mean horizontal wind, the wind field is assumed to have linear horizontal
548 velocity and constant hydrometeor vertical speed across the total scan circle. These assumptions
549 tend to hold well in stratiform precipitation regions like that in the current dataset since these
550 mesoscale regions contain weak vertical velocities and winds that vary slowly over horizontal
551 distances. In order to capture convective-scale features, one of the three-dimensional wind
552 retrieval methods must be used.

553

554 **7. Conclusions**

555 In this paper, the coplane method for dual-Doppler wind retrieval (Armijo 1969; Miller
556 and Strauch 1974) is adapted to the downward pointing conically scanning technique of the
557 NASA HIWRAP airborne radar. The coplane method takes the radar observations and solves for
558 the three-dimensional winds using a simple interpolation and integration approach. This
559 approach locally solves for the wind field which is in contrast to the global optimization
560 (variational) method described by Guimond et al. (2014). In order to retrieve the unobserved

561 wind component (U_α) at all points, observations must exist at all points in the domain. The main
562 advantage of the coplane method is the transparency of its calculations. The interpolation and
563 solving processes are discretely and separately calculated, which allows for exact calculation of
564 wavelength resolution and tracing of source data from the solution.

565 Simulated radar observations of a model hurricane were used to test the coplane method
566 and compare to the variational method. The coplane method retrieved the wind field with small
567 errors relative to the wind speed magnitudes. Compared to the variational method, the coplane
568 method had lower errors in the cross-track component (u) and vertical component (w) fields,
569 while the variational method had lower errors in the along-track component (v) field. For the
570 coplane method, the accuracy of u relied on the accuracy of the U_α boundary initializations.
571 Where U_α was initialized sufficiently well, u remained accurate across the span of the domain.
572 Where U_α was not well initialized, errors in u propagate along the curved integration path,
573 creating an easily recognizable error signature. The w component, which is also derived from U_α ,
574 produced errors at the domain edges along curved integration paths with insufficiently initialized
575 U_α . The error patterns for the variational field were different, showing errors in u and w that
576 grew toward the edges of the domain at all altitudes.

577 The coplane and variational methods were applied to HIWRAP observations collected
578 during the NASA HS3 campaign. Both techniques produced errors in the retrieval that appeared
579 in patterns similar to the errors in the simulated radar retrieval. Prior knowledge of the error
580 patterns expected from each method allowed for this recognition of retrieval errors in the HS3
581 retrieval. As a local solver, the errors in the coplane analysis are easily traced to the certain
582 observations and/or U_α initializations. Unlike the transparency of a local solver, the errors
583 arrived with the global solver cannot be explicitly traced to certain observations or calculations

584 since the solution at a particular location depends on the solution everywhere. Additionally, since
585 the coplane method employs the Barnes filter, the corresponding response function provides the
586 exact minimum resolvable wavelength of the final solution. The minimum resolvable wavelength
587 for the variational method cannot be exactly calculated since the interpolation filter and
588 Laplacian smoother are constraints on the optimization rather than exact calculations.

589 The coplane technique's ability to transparently trace the exact calculations from the raw
590 observations to the final solution is highly beneficial when making scientific interpretations. This
591 ability is necessary to more adequately analyze small-scale features in tropical cyclones, such as
592 rotating deep convection (Hendricks et al. 2004; Montgomery et al. 2006; Sanger et al. 2014). A
593 key skill for radar analyses is being able to separate true meteorological signals from non-
594 meteorological signals such as noise or data contamination that has bypassed the data quality
595 control process. Once a solution is obtained, quirky regions in the final solution can be
596 ambiguous as to whether they are true representations of small-scale features. After easily
597 pinpointing the raw observations that were used to create the solution, the user can better assess
598 the reality of the observations taken, and corrections can subsequently be implemented or not
599 implemented. In the variational method, these anomalous measurements would be smoothed and
600 impact the entire retrieval, which would either dilute the small-scale signal or incorporate
601 erroneous data in the solution. The coplane method can prevent incorrect scientific
602 interpretations of inherently wrong solutions or strengthen confidence in the conclusions based
603 on the observations. Given the wind component error analyses for both retrieval methods, the
604 option to trace solution calculations with the coplane analysis is provided to the user with
605 minimal cost to the accuracy of the overall solution.

606 Future work will use the coplane analysis for scientific research of observations from the
607 HS3 field campaign and other planned campaigns using the HIWRAP radar. This technique can
608 also be used to analyze tail Doppler radar data from tropical cyclones documented in peer-
609 reviewed work (e.g. Marks and Houze 1984; Reasor et al. 2009; Houze et al. 2009; Bell and
610 Montgomery 2010) as well as future field campaigns. In locations directly beneath the aircraft,
611 the geometry of the tail Doppler radar observations is compatible with the coplane technique.
612 These additional analyses would be especially useful here as these locations are particularly
613 troublesome for capturing small-scale features with the global optimization technique.

614

615 **Acknowledgements.** We thank Matthew McLinden, Lihua Li, Martin Perrine, Jaime Cervantes,
616 and Ed Zenker for their engineering support and data processing for the HIWRAP radar. We
617 thank Shuyi Chen for providing the model output used in this study. We also thank the three
618 anonymous reviewers of this manuscript. The first author conducted this research at the NASA
619 Goddard Space Flight Center under the support of the NASA Postdoctoral Program (NPP)
620 conducted by Oak Ridge Associated Universities (ORAU).

621

622

623

624

625

626

627

628

629
630
631
632
633
634
635
636
637
638
639
640
641
642
643
644
645
646
647
648
649
650

References

Armijo, L., 1969: A theory for the determination of wind and precipitation velocities with Doppler radars. *J. Atmos. Sci.*, **26**, 570-573.

Barnes, S. L., 1973: Mesoscale objective analysis using weighted time-series observations. NOAA Tech. Memo. ERL NSSL-62, National Severe Storms Laboratory, Normal, OK 73069, 60 pp. [NTIS COM-73-10781].

Bell, M. M., and M. T. Montgomery, 2010: Sheared deep vortical convection in pre-depression Hagupit during TCS08. *Geophys. Res. Lett.*, **37**, L06802, doi:10.1029/2009GL042313.

Bousquet, O., and M. Chong, 1998: A multiple-Doppler synthesis and continuity adjustment technique (MUSCAT) to recover wind components from Doppler radar measurements. *J. Atmos. Oceanic Technol.*, **15**, 343-359.

Braun, S. A., and Coauthors, 2013: NASA's Genesis and Rapid Intensification Processes (GRIP) Field Experiment. *Bull. Amer. Meteor. Soc.*, **94**, 345–363.

Browning, K. A., and R. Wexler, 1968: The determination of kinematic properties of a wind field using Doppler radar. *J. Appl. Meteor.*, **7**, 105-113.

Chong, M., and J. Testud, 1996: Three-dimensional air circulation in a squall line from airborne dual-beam Doppler radar data: A test of coplane methodology software. *J. Atmos. Oceanic Technol.*, **13**, 36-53.

Dazhang, T., S. G. Geotis, R. E. Passarelli Jr. , A. L. Hansen, ad C. I. Frush, 1984: Evaluation of an alternating –PRF method for extending the range of unambiguous Doppler velocity. Preprints, 22d *Conf. On Radar Meteorology*, Zurich, Switzerland. Amer Meteor. Soc., 523-527.

651 Doviak, R. J., P. S. Ray, R. G. Strauch, and L. J. Miller, 1976: Error estimation in wind fields
652 derived from dual-Doppler radar measurement. *J. Appl. Meteor.*, **15**, 868-878.

653 Gamache, J. F., 1997: Evaluation of a fully three-dimensional variational Doppler analysis
654 technique. Preprints, *28th Conf. on Radar Meteorology*, Austin, TX, Amer. Meteor. Soc.,
655 422-423.

656 Gamache, J. F., F. D. Marks Jr., and F. Roux, 1995: Comparison of three airborne Doppler
657 sampling techniques with airborne in situ wind observations in Hurricane Gustav (1990). *J.*
658 *Atmos. Oceanic Technol.*, **12**, 171-181.

659 Gao, J., M. Xue, A. Shapiro, and K. K. Droegemeier, 1999: A variational method for the analysis
660 of three-dimensional wind fields from two Doppler radars. *Mon. Wea. Rev.*, **127**, 2128-2142.

661 Guimond, S. R., L. Tian, G. M. Heymsfield, and S. J. Frasier, 2014: Wind retrieval algorithms
662 for the IWRAP and HIWRAP airborne Doppler radars with application to hurricanes. *J.*
663 *Atmos. Oceanic Technol.*, **31**, 1189 – 1215.

664 Hendricks, E. A., M. T. Montgomery, and C. A. Davis, 2004: The role of “vortical” hot towers in
665 the formation of Tropical Cyclone Diana (1984). *J. Atmos. Sci.*, **61**, 1209–1232.

666 Heymsfield, G. M., L. Tian, A. J. Heymsfield, L. Li, S. Guimond, 2010: Characteristics of Deep
667 Tropical and Subtropical Convection from Nadir-Viewing High-Altitude Airborne Doppler
668 Radar. *J. Atmos. Sci.*, **67**, 285–308.

669 Hildebrand, P. H., and Coauthors, 1996: The ELDORA/ASTRAIA airborne Doppler weather
670 radar: High-resolution observations from TOGA COARE. *Bull. Amer. Meteor. Soc.*, **77**, 213-
671 232.

672 Houze, R. A., Jr., 1997: Stratiform precipitation in regions of convection: A meteorological
673 paradox? *Bull. Amer. Meteor. Soc.*, **78**, 2179-2196.

674 Houze, R. A., Jr., W.-C. Lee, and M. M. Bell, 2009: Convective contribution to the genesis of
675 Hurricane Ophelia (2005). *Mon. Wea. Rev.*, **137**, 2778–2800.

676 Jordan, C. L., 1958: Mean soundings for the West Indies area. *J. Atmos.Sci.*, **15**, 91-97.

677 Jorgensen, D. P., 1984: Mesoscale and convective-scale characteristics of mature hurricanes. Part
678 I: General observations by research aircraft. *J. Atmos.Sci.*, **41**, 1268-1285.

679 Jorgensen, D. P., and J. D. DuGranrut, 1991: A dual-beam technique for deriving wind fields
680 from airborne Doppler radar. *Preprints, 25th International Conf. Radar Meteor.*, Amer.
681 Meteor. Soc., 458-461.

682 Jorgensen, D. P., P. H. Hildebrand, and C. L. Frush, 1983: Feasibility test of an airborne pulse-
683 Doppler meteorological radar. *J. Climate Appl. Meteor.*, **22**, 744-757.

684 Klimowski, B. A., and J. D. Marwitz, 1992: The synthetic Dual-Doppler analysis technique. *J.*
685 *Atmos. Oceanic Technol.*, **9**, 728-745.

686 Koch, S. E., M. desJardins, and P. J. Kocin, 1983: An interactive Barnes objective map analysis
687 scheme for use with satellite and conventional data. *J. Climate Appl. Meteor.*, **22**, 1487-1503.

688 Lee, W.-C., P. Dodge, F. D. Marks Jr., and P. H. Hildebrand, 1994: Mapping of airborne
689 Doppler radar data. *J. Atmos. Oceanic Technol.*, **11**, 572-578.

690 Lhermitte, R. M., 1971: Probing of atmospheric motion by airborne pulse-Doppler radar
691 techniques. *J. Appl. Meteor.*, **10**, 235-246.

692 Lhermitte, R. M., and D. Atlas, 1961: Precipitation motion by pulse Doppler radar. Proc.
693 Weather Radar Conf., 9th, 1961, pp. 218-223.

694 Li, L., and Coauthors, 2014: Development of the NASA High-altitude Imaging Wind and Rain
695 Airborne Profiler (HIWRAP). *IEEE Trans. Geosci. Remote Sensing*, in review.

696 Marks, F. D., Jr., and R. A. Houze Jr., 1984: Airborne Doppler radar observations in Hurricane
697 Debby. *Bull. Amer. Meteor. Soc.*, **65**, 569-582.

698 Miller, L. J., and R. G. Strauch, 1974: A dual Doppler radar method for the determination of
699 wind velocities within precipitating weather systems. *Remote Sensing of Environment*, **3**,
700 219-235.

701 Mohr, C. G., L. J. Miller, R. L. Vaughan, and H. W. Frank, 1986: The merger of mesoscale
702 datasets into a common Cartesian format for efficient and systematic analyses. *J. Atmos.*
703 *Oceanic Technol.*, **3**, 143-161.

704 Montgomery, M. T., M. M. Bell, S. D. Aberson, and M. L. Black, 2006: Hurricane Isabel (2003):
705 New insights into the physics of intense storms. Part I: Mean vortex structure and maximum
706 intensity estimates. *Bull. Amer. Meteor. Soc.*, **87**, 1335–1347.

707 Reasor, P. D., M. D. Eastin, and J. F. Gamache, 2009: Rapidly intensifying Hurricane Guillermo
708 (1997). Part I: Low-wavenumber structure and evolution. *Mon. Wea. Rev.*, **137**, 603-631.

709 Sanger, N. T., M. T. Montgomery, R. K. Smith, and M. M. Bell 2014: An observational study of
710 tropical cyclone spinup in Supertyphoon Jangmi from 24-27 Sep. *Mon. Wea. Rev.*, **142**, 3-28.

711 Testud, J., P. H. Hildebrand, and W.-C. Lee, 1995: A procedure to correct airborne Doppler radar
712 data for navigation errors using the echo returned from the earth's surface. *J. Atmos. Oceanic*
713 *Technol.*, **12**, 800-820.

714 Tian, L., G. M. Heymsfield, S. Guimond, and L. Li, 2015: VAD and dual-Doppler analysis of
715 Doppler velocity for HIWRAP. *J. Appl. Meteor.*, in review.

716

717

718

719
720
721
722
723
724
725
726
727
728
729
730
731
732
733
734
735
736
737
738

Tables

Table 1. Parameters used for the variational dual-Doppler retrieval. Each parameter is explained in detail in Guimond et al. (2014).

Shape parameter γ	0.75
Along-track sampling s	560 m
Smoothing factor β	4
Weighting factor α_M	2×2000^2
Weighting factor α_S	For simulated data: 0 For real data: 0.4×2000^4

Figure Captions

739

740

741 **Figure 1.** Schematic showing the scanning technique of the HIWRAP radar in a track-following
742 Cartesian coordinate frame (X_b, Y_b, Z_t) . Two beams each with Ku and Ka band point downward at
743 two angles and scan conically around a vertical axis. For a stationary radar and plane at its
744 typical altitude of 18.5 km, the outermost beam scans a circle at the surface ($Z=0$) with an
745 approximate diameter of 30 km.

746

747 **Figure 2.** Cylindrical coordinate system used for the coplane dual-Doppler retrieval from
748 HIWRAP observations. P is the position of the target in the cylindrical coordinate system
749 defined by the radius (ρ), coplane angle (α), and flight track distance (Y). The red dashed lines
750 and red arrows represent line segments and vectors, respectively, along the radar beam. The
751 black dashed line and black arrows within the coplane represent a line segment and vectors in the
752 cylindrical coordinate system. The symbols r_1 and r_2 are the ranges of the target from the radar
753 positions at Y_1 and Y_2 . β_1 and β_2 are the positive angles between the ranges and the radius ρ . V_{r1}
754 and V_{r2} are the radial Doppler velocities at point P, and U_ρ and U_Y are the corresponding
755 cylindrical coordinate velocity components in the coplane. The axes X_t, Y , and Z_t define the
756 corresponding track-following Cartesian coordinate frame where Y_t is coincident with Y . Figure
757 adapted from Tian et al. (2015).

758

759 **Figure 3.** a) The separation angle β as a function of the coplane angle α for the inner beam
760 (dashed black) and the outer beam (solid black). b) Variance (σ^2) of the U_Y (red) and U_ρ (blue)
761 wind components due to Doppler estimate error as a function of the coplane angle α . Variances

762 are calculated for the Ka band inner (red dashed and blue dashed) and outer (red solid and blue
763 solid) beams.

764

765 **Figure 4.** Diagram of the cylindrical grid (ρ, α) along a given Y location. Red lines indicate the
766 boundary condition locations for initialization of the U_α wind component. Blue arrows indicate
767 the integration directions for retrieving the U_α wind component. The shaded region shows the
768 area initialized by the surface boundary condition.

769

770 **Figure 5.** Plan view of model reflectivity at 2 km altitude. The data are HIWRAP radar simulator
771 observations of a model simulation of Hurricane Rita at peak strength.

772

773 **Figure 6.** a) Infrared satellite imagery of Hurricane Ingrid (2014) with the flight track from 15
774 Sep 2014 of the NASA Global Hawk AV1 overlain in yellow. A black 'X' marks the best track
775 storm center b) The 1.5-km Ka band outer beam reflectivity observed by HIWRAP along the
776 flight track from a). Observations were taken from 1836-1900Z. c) Nadir view of Ka band outer
777 beam reflectivity. The graph origin is the eastern end of the plan view reflectivity from b).

778

779 **Figure 7.** a) The coplane angle α as a function of rotation angle calculated from Eq. (18).

780 Results from the inner beam (red) and outer beam (black) are shown. b) RMS errors of U_α in the
781 nadir boundary condition estimate for varying rotation angles (dots) and cross-track distance
782 between outer beam locations for varying rotation angles (dashed line).

783

784 **Figure 8.** U_a wind component at nadir retrieved from the radar simulator data using the coplane
785 analysis. Deviations from the model truth are shown in black contours at intervals of 2 m s^{-1} .
786 Dashed lines are negative values beginning at -2 m s^{-1} and solid lines are positive values
787 beginning at 2 m s^{-1} . See text for details.

788

789 **Figure 9.** Root-mean-square (RMS) errors of the two retrieval methods. Errors from the coplane
790 analysis are shown for the a) cross-track (u), b) along-track (v), and c) vertical (w) wind
791 components. Errors from the variational analysis are shown in d) – f) for the same wind
792 components. Error fields are averaged along the flight track. Overall RMS and relative-RMS
793 errors are also given (in m s^{-1} and %, respectively).

794

795 **Figure 10.** RMS errors of the coplane analysis for the a) cross-track (u) and b) vertical (w) wind
796 components averaged along the flight track. This analysis uses nadir and lower-bound boundary
797 conditions given by the model truth field. Overall RMS and relative-RMS errors are also given
798 (in m s^{-1} and %, respectively).

799

800 **Figure 11.** Nadir view of the a) u , b) v , and c) w wind components as derived by the coplane
801 analysis of the HIWRAP observations seen in Fig. 6. The variational analysis wind components
802 are shown in d) – f).

803

804 **Figure 12.** Cross-track view of the a) u , b) v , and c) w wind components as derived by the
805 coplane analysis of the HIWRAP observations. The variational analysis wind components are
806 shown in d) – f). This cross section is taken at $Y_t=160 \text{ km}$ from Fig. 12.

807

808 **Figure 13.** Nadir view of the a) u and c) v wind components as derived by the vertical azimuth

809 display (VAD) analysis of the HIWRAP observations seen in Fig. 6.

810

811

812

813

814

815

816

817

818

819

820

821

822

823

824

825

826

827

828

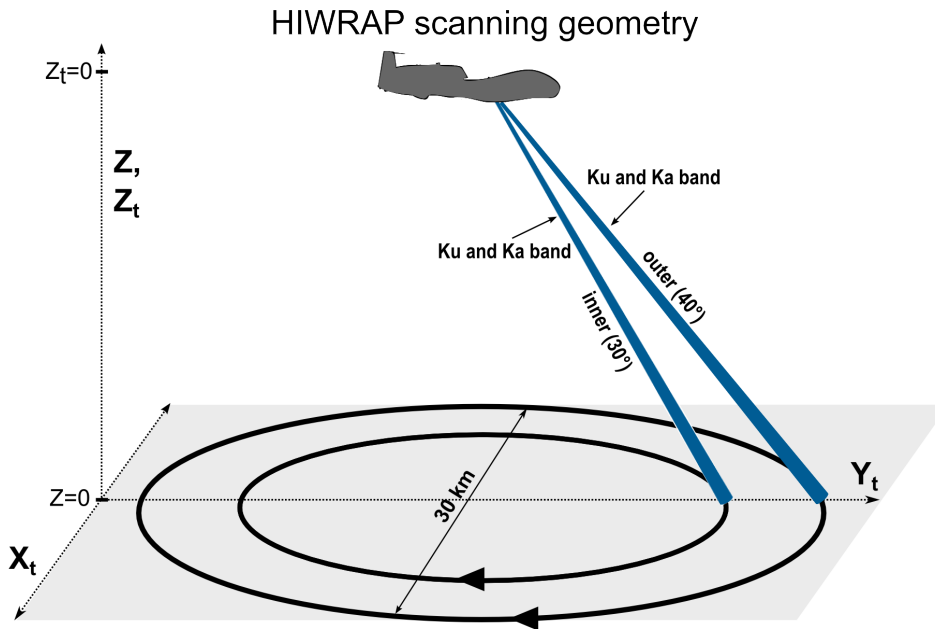
829

830 **Figures**

831

832

833



834

835

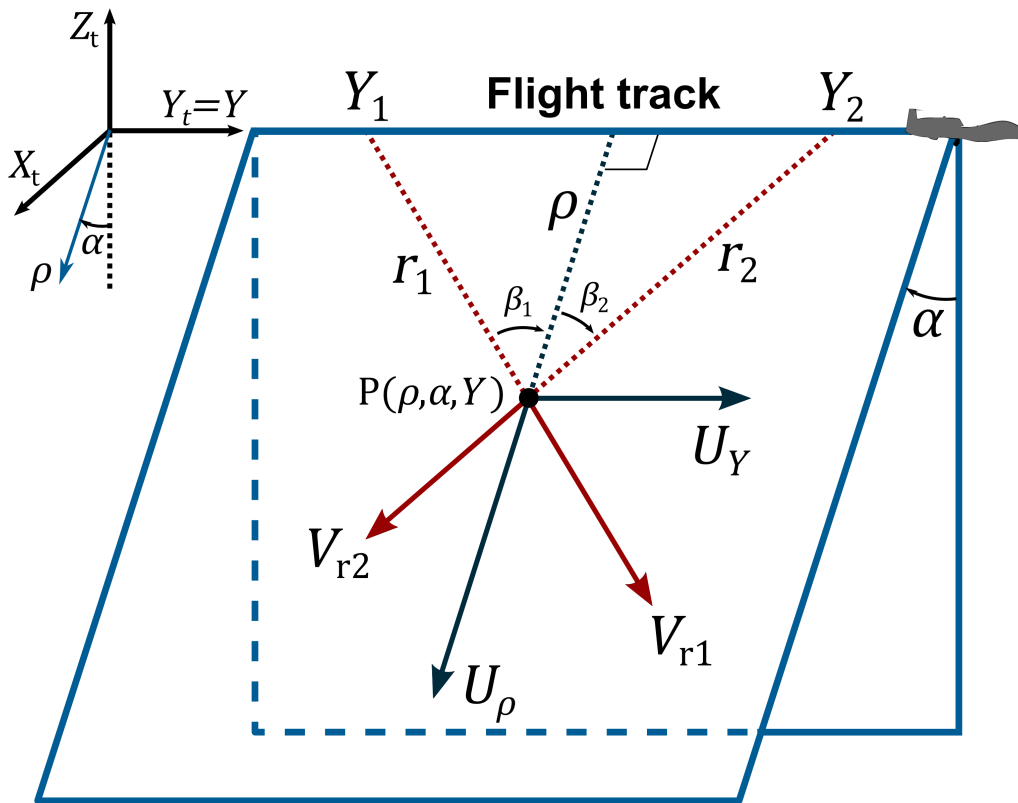
836 **Figure 1.** Schematic showing the scanning technique of the HIWRAP radar in a track-following
837 Cartesian coordinate frame (X_t , Y_t , Z_t). Two beams each with Ku and Ka band point downward at
838 two angles and scan conically around a vertical axis. For a stationary radar and plane at its
839 typical altitude of 18.5 km, the outermost beam scans a circle at the surface ($Z=0$) with an
840 approximate diameter of 30 km.

841

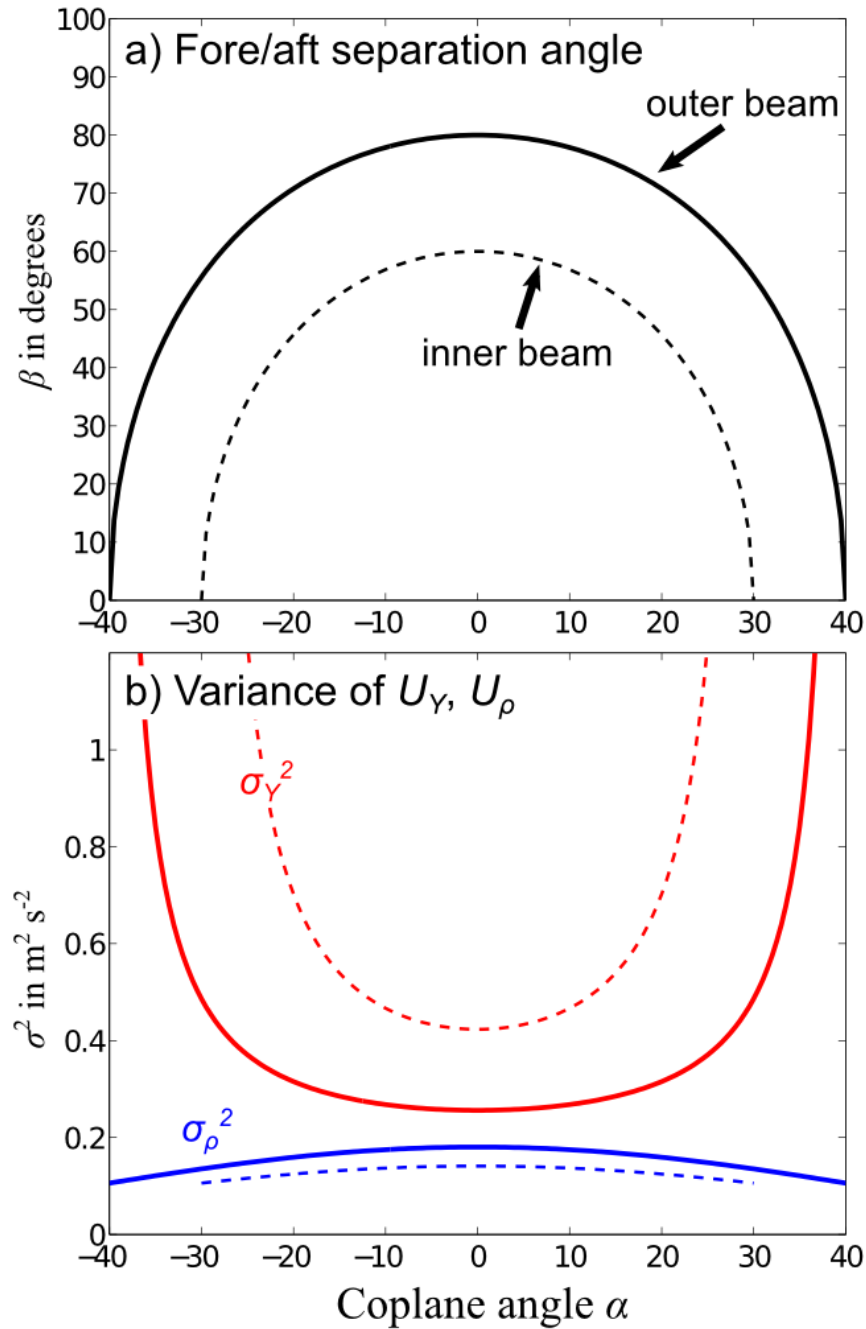
842

843

844



845
 846 **Figure 2.** Cylindrical coordinate system used for the coplane dual-Doppler retrieval from
 847 HIWRAP observations. P is the position of the target in the cylindrical coordinate system
 848 defined by the radius (ρ), coplane angle (α), and flight track distance (Y). The red dashed lines
 849 and red arrows represent line segments and vectors, respectively, along the radar beam. The
 850 black dashed line and black arrows within the coplane represent a line segment and vectors in the
 851 cylindrical coordinate system. The symbols r_1 and r_2 are the ranges of the target from the radar
 852 positions at Y_1 and Y_2 . β_1 and β_2 are the positive angles between the ranges and the radius ρ . V_{r1}
 853 and V_{r2} are the radial Doppler velocities at point P, and U_ρ and U_Y are the corresponding
 854 cylindrical coordinate velocity components in the coplane. The axes X_t , Y , and Z_t define the
 855 corresponding track-following Cartesian coordinate frame where Y_t is coincident with Y . Figure
 856 adapted from Tian et al. (2015).



857

858 **Figure 3.** a) The separation angle β as a function of the coplane angle α for the inner beam

859 (dashed black) and the outer beam (solid black). b) Variance (σ^2) of the U_Y (red) and U_ρ (blue)

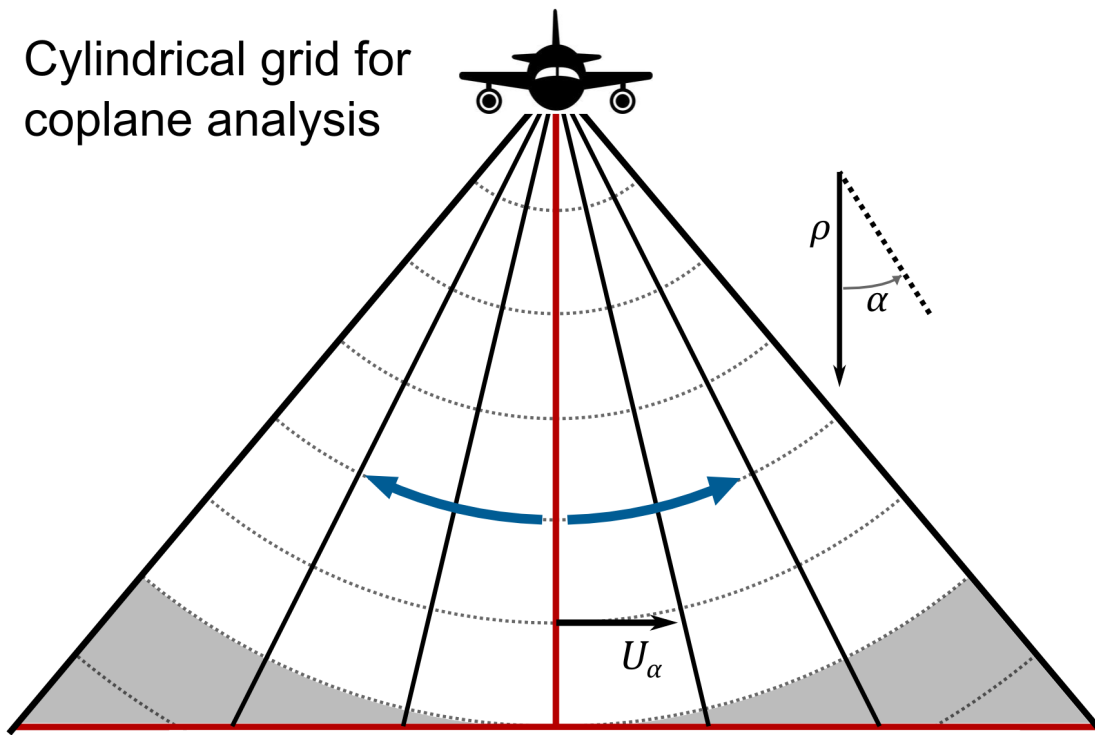
860 wind components due to Doppler estimate error as a function of the coplane angle α . Variances

861 are calculated for the Ka band inner (red dashed and blue dashed) and outer (red solid and blue

862 solid) beams.

863

864



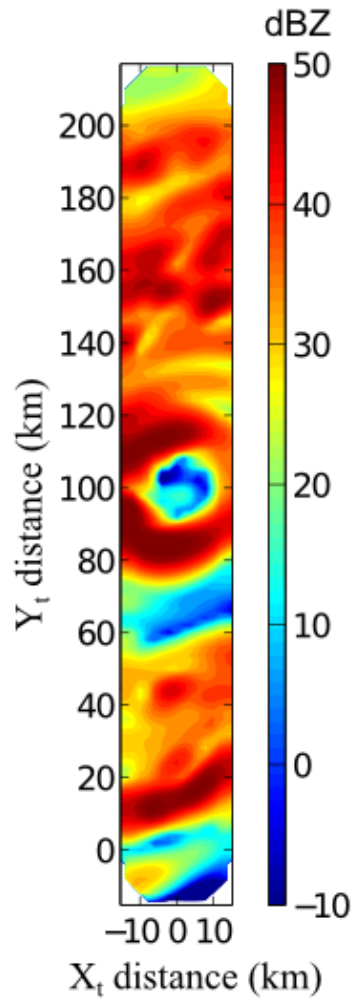
865

866 **Figure 4.** Diagram of the cylindrical grid (ρ, α) along a given Y location. Red lines indicate the
867 boundary condition locations for initialization of the U_α wind component. Blue arrows indicate
868 the integration directions for retrieving the U_α wind component. The shaded region shows the
869 area initialized by the surface boundary condition.

870

871

872



873

874 **Figure 5.** Plan view of model reflectivity at 2 km altitude. The data are HIWRAP radar simulator
875 observations of a model simulation of Hurricane Rita at peak strength.

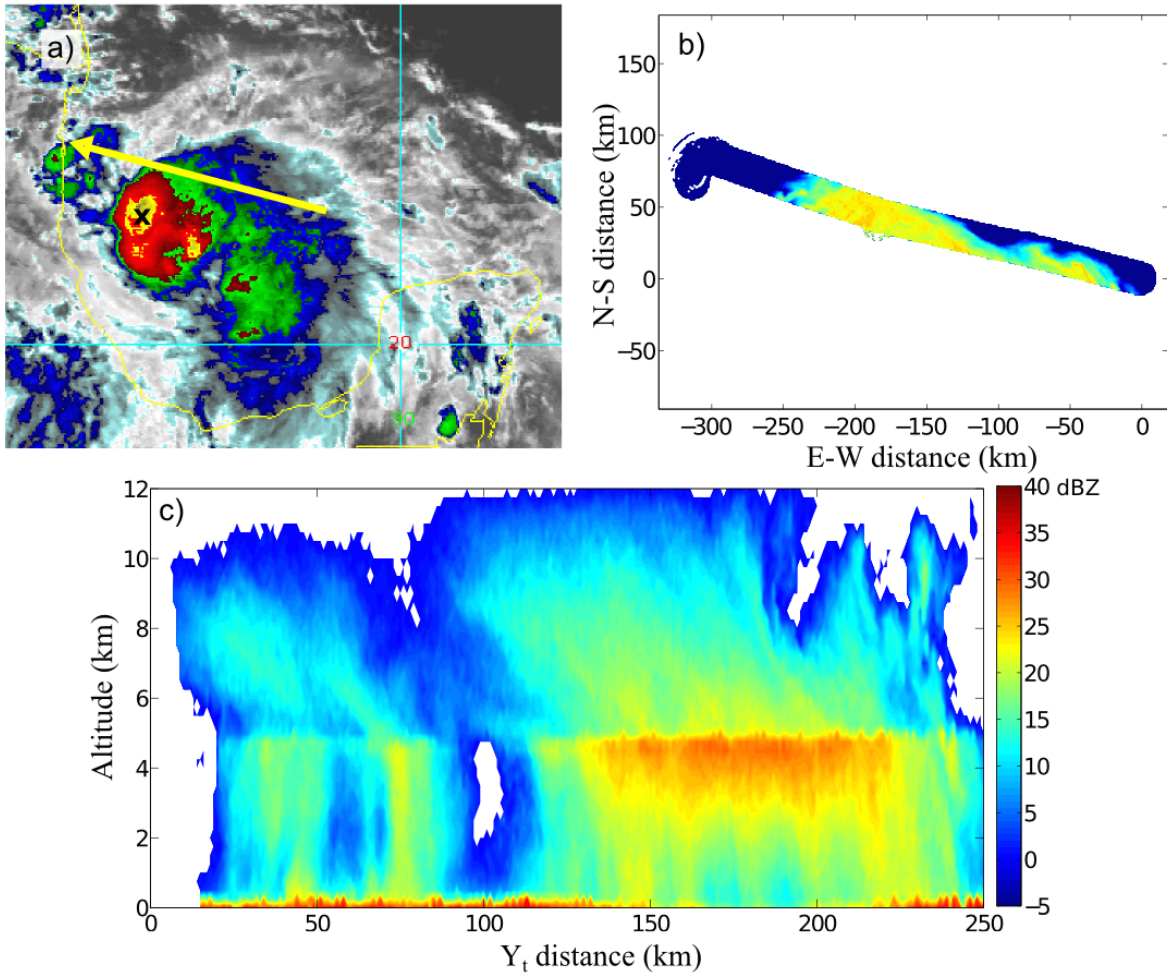
876

877

878

879

880



881

882

883 **Figure 6.** a) Infrared satellite imagery of Hurricane Ingrid (2014) with the flight track from 15

884 Sep 2014 of the NASA Global Hawk AV1 overlain in yellow. A black 'X' marks the best track

885 storm center b) The 1.5-km Ka band outer beam reflectivity observed by HIWRAP along the

886 flight track from a). Observations were taken from 1836-1900Z. c) Nadir view of Ka band outer

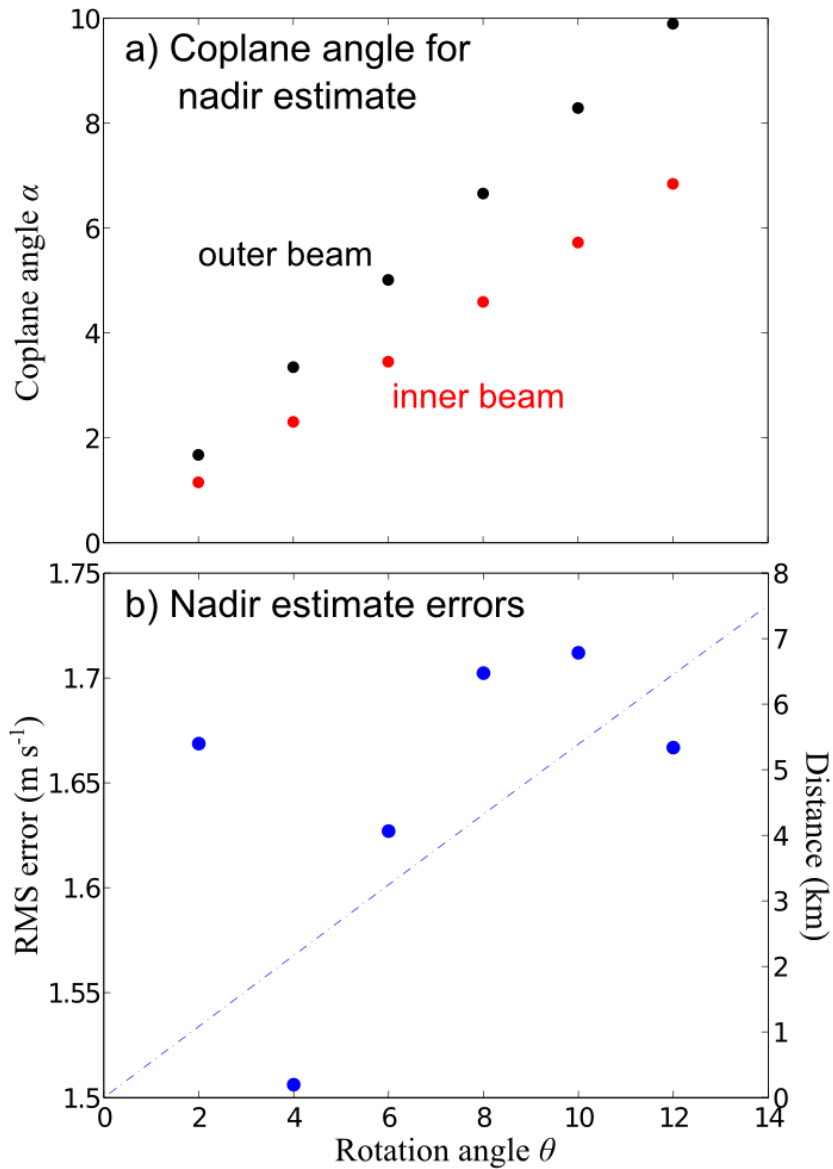
887 beam reflectivity. The graph origin is the eastern end of the plan view reflectivity from b).

888

889

890

891



892

893 **Figure 7.** a) The coplaner angle α as a function of rotation angle calculated from Eq. (18).

894 Results from the inner beam (red) and outer beam (black) are shown. b) RMS errors of U_α in the

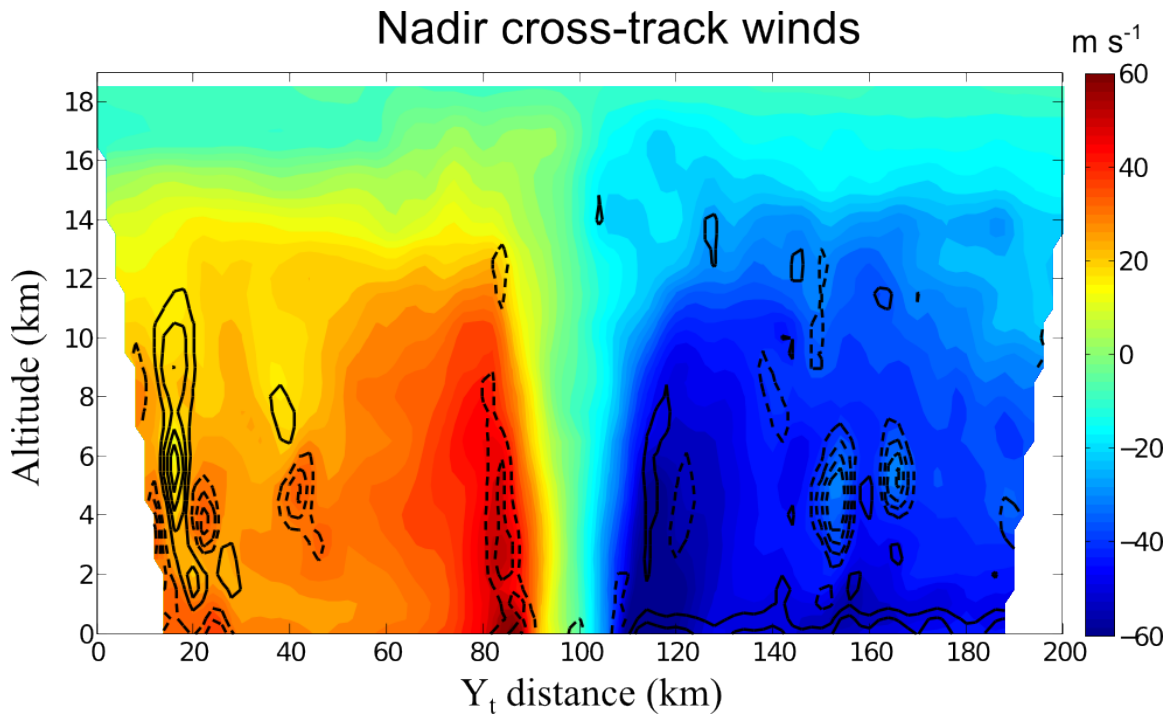
895 nadir boundary condition estimate for varying rotation angles (dots) and cross-track distance

896 between outer beam locations for varying rotation angles (dashed line).

897

898

899



900

901 **Figure 8.** U_α wind component at nadir retrieved from the radar simulator data using the coplane

902 analysis. Deviations from the model truth are shown in black contours at intervals of 2 m s^{-1} .

903 Dashed lines are negative values beginning at -2 m s^{-1} and solid lines are positive values

904 beginning at 2 m s^{-1} . See text for details.

905

906

907

908

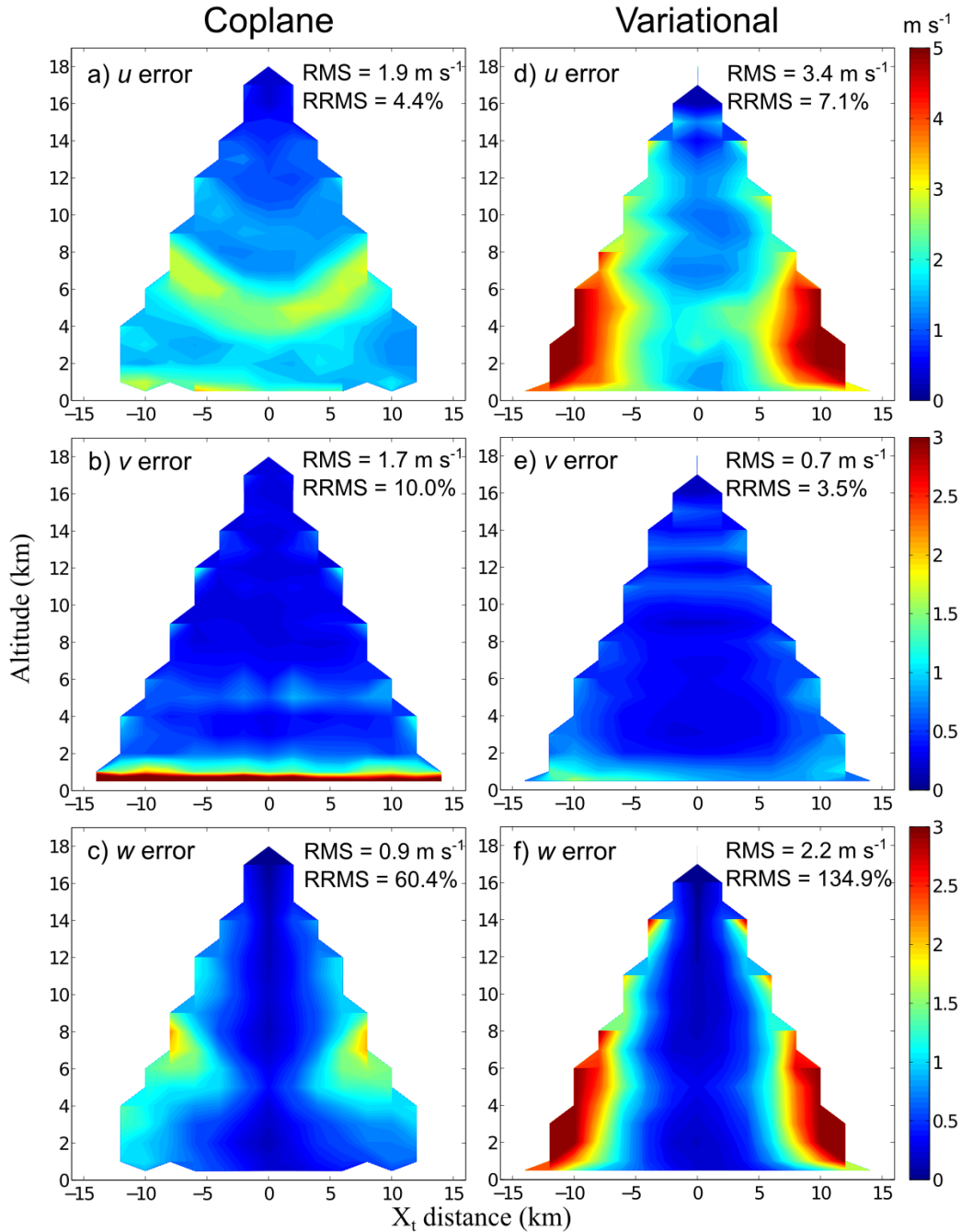
909

910

911

912

913



914

915 **Figure 9.** Root-mean-square (RMS) errors of the two retrieval methods. Errors from the coplane

916 analysis are shown for the a) cross-track (u), b) along-track (v), and c) vertical (w) wind

917 components. Errors from the variational analysis are shown in d) – f) for the same wind

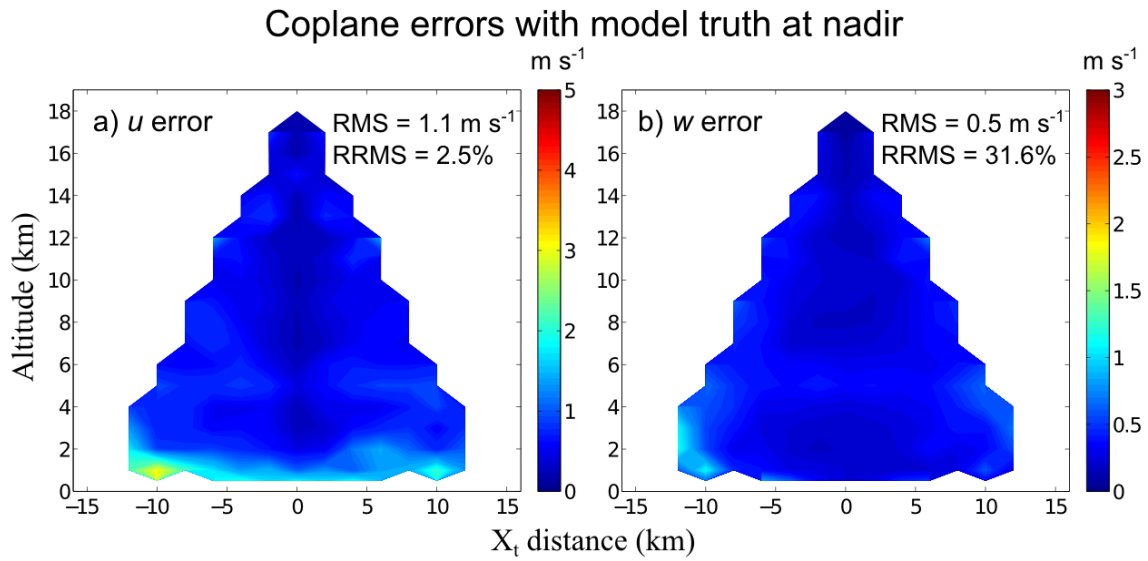
918 components. Error fields are averaged along the flight track. Overall RMS and relative-RMS

919 errors are also given (in m s^{-1} and %, respectively).

920

921

922



923

924 **Figure 10.** RMS errors of the coplane analysis for the a) cross-track (u) and b) vertical (w) wind
925 components averaged along the flight track. This analysis uses nadir and lower-bound boundary
926 conditions given by the model truth field. Overall RMS and relative-RMS errors are also given
927 (in m s^{-1} and %, respectively).

928

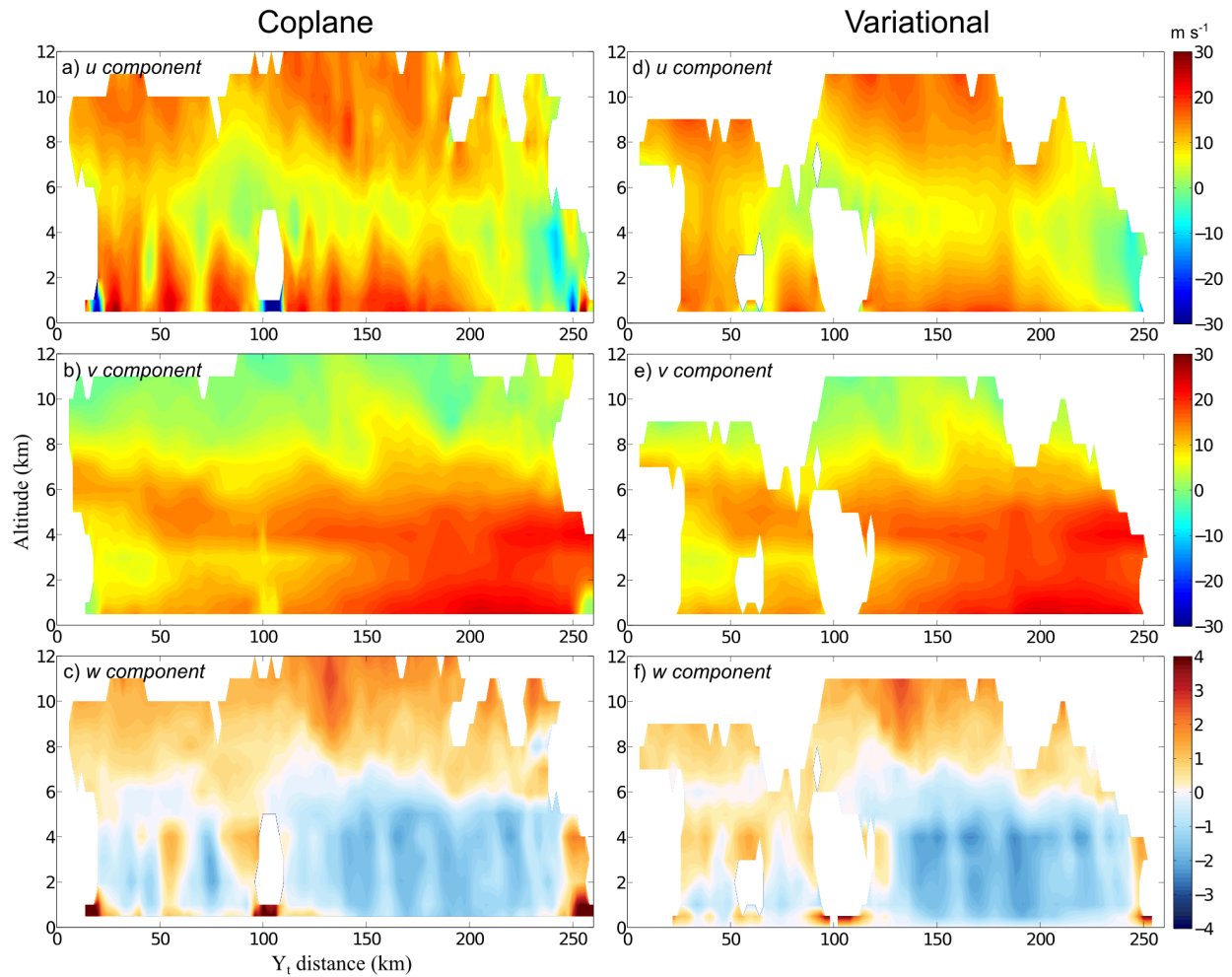
929

930

931

932

933



934

935

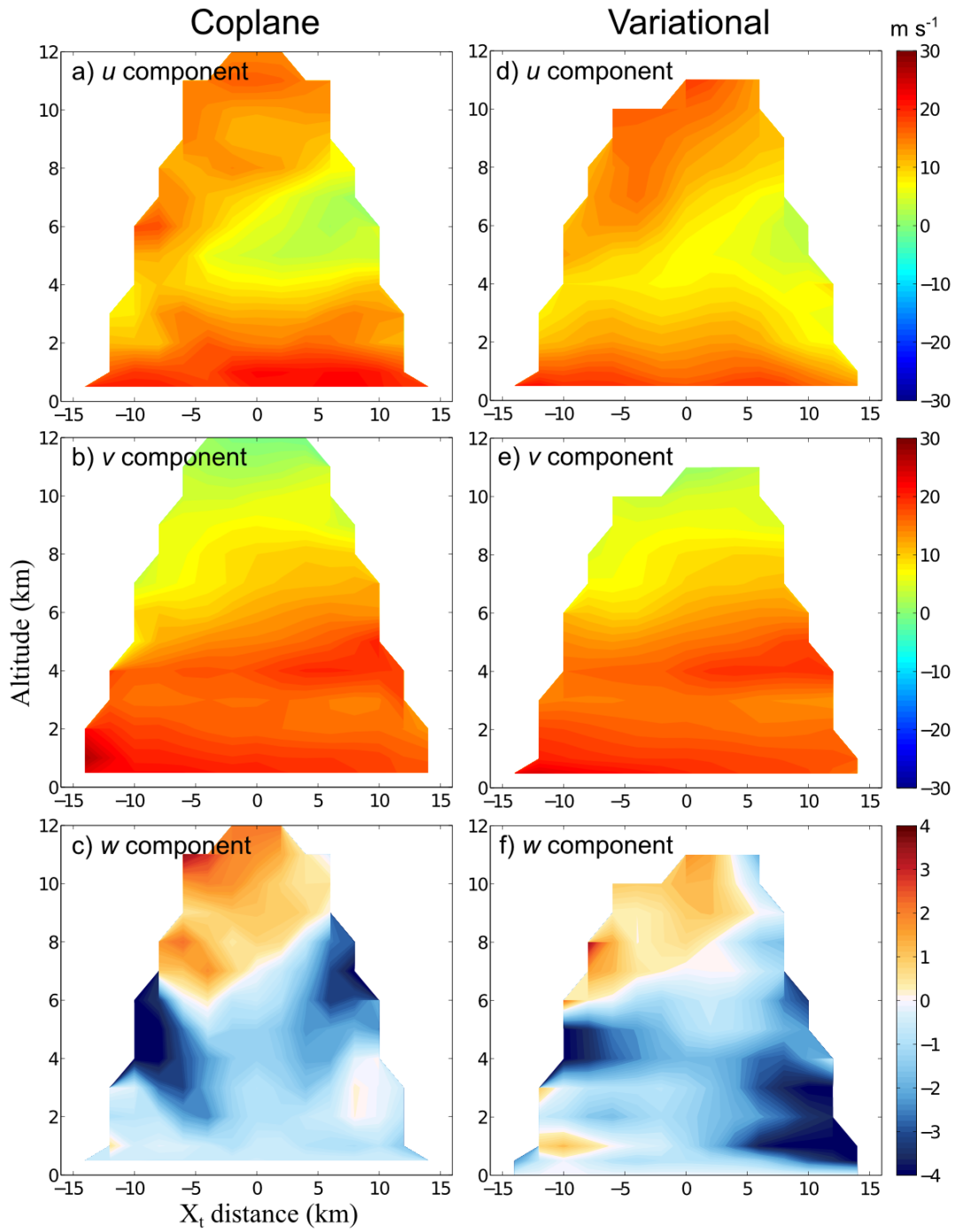
936 **Figure 11.** Nadir view of the a) u , b) v , and c) w wind components as derived by the coplane

937 analysis of the HIWRAP observations seen in Fig. 6. The variational analysis wind components

938 are shown in d) – f).

939

940

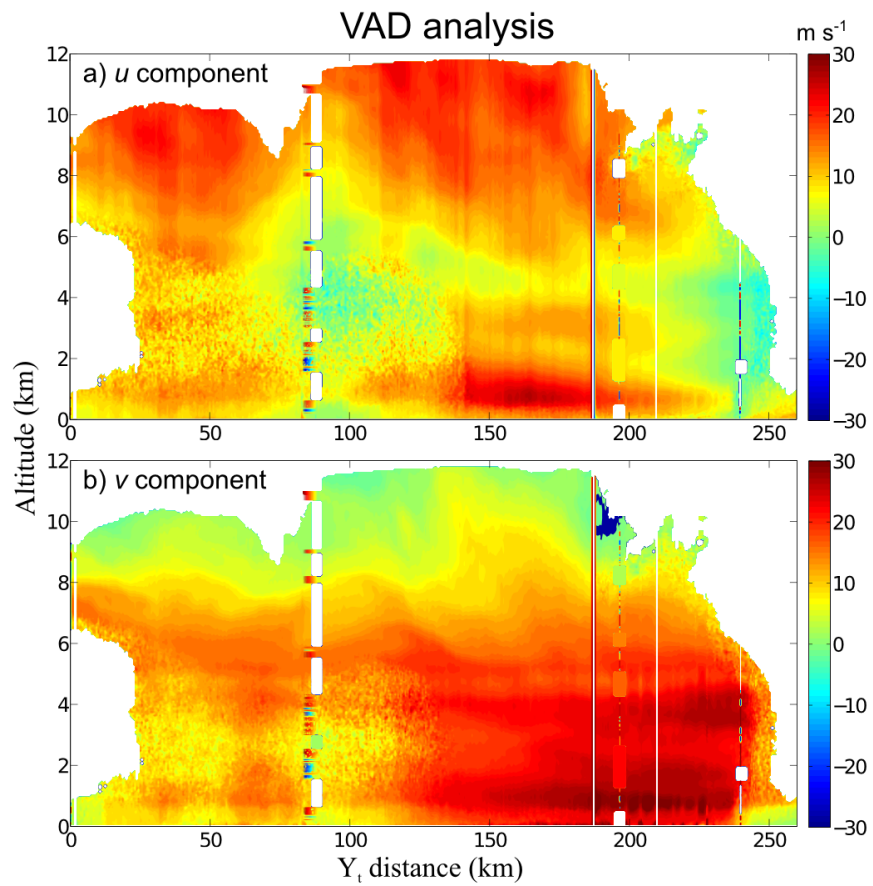


941

942 **Figure 12.** Cross-track view of the a) u , b) v , and c) w wind components as derived by the
 943 coplane analysis of the HIWRAP observations. The variational analysis wind components are
 944 shown in d) – f). This cross section is taken at $Y_t=160$ km from Fig. 12.

945

946



947

948

949 **Figure 13.** Nadir view of the a) u and c) v wind components as derived by the vertical azimuth
950 display (VAD) analysis of the HIWRAP observations seen in Fig. 6.